Experimental and computational analysis of thermal environment in the operation of HfO_2 memristors

Cite as: AIP Advances **10**, 035127 (2020); https://doi.org/10.1063/1.5141347
Submitted: 04 December 2019 • Accepted: 07 March 2020 • Published Online: 24 March 2020

Darshan G. Pahinkar, Pradip Basnet, Matthew P. West, et al.

Experimental and computational analysis of thermal environment in the operation of HfO_2 memristors

Cite as: AIP Advances 10, 035127 (2020); doi: 10.1063/1.5141347
Submitted: 4 December 2019 • Accepted: 7 March 2020 •
Published Online: 24 March 2020

Darshan G. Pahinkar,[1,a)] Pradip Basnet,[2] Matthew P. West,[2] Bill Zivasatienraj,[3] Alex Weidenbach,[3] W. Alan Doolittle,[3] Eric Vogel,[2] and Samuel Graham[4]

AFFILIATIONS

[1]Department of Mechanical and Civil Engineering, Florida Institute of Technology, Melbourne, Florida 32940, USA
[2]School of Materials Science and Engineering, 800 Ferst Drive NW, Atlanta, Georgia 30332, USA
[3]Department of Electrical and Computer Engineering, 800 Ferst Drive NW, Atlanta, Georgia 30332, USA
[4]George W. Woodruff School of Mechanical Engineering, Georgia Institute of Technology, 800 Ferst Drive NW, Atlanta, Georgia 30332, USA

[a)]Author to whom correspondence should be addressed: dpahinkar@fit.edu

ABSTRACT

Neuromorphic computation using nanoscale adaptive oxide devices or memristors is a very promising alternative to the conventional digital computing framework. Oxides of transition metals, such as hafnium (HfO_x), have been proven to be excellent candidate materials for these devices, because they show non-volatile memory and analog switching characteristics. This work presents a comprehensive study of the transport phenomena in HfO_x based memristors and involves the development of a fully coupled electrothermal and mass transport model that is validated with electrical and thermal metrology experiments. The fundamental transport mechanisms in HfO_x devices were analyzed together with the local and temporal variation of voltage, current, and temperature. The effect of thermal conductivity of substrate materials on the filament temperature, voltage ramp rate, and set/reset characteristics was investigated. These analyses provide insight into the switching mechanisms of these oxides and allow for the prediction of the effect of device architecture on switching behavior.

INTRODUCTION

As the development of conventional digital computing techniques became saturated due to scaling limits and difficulty in removing heat, other alternatives such as neuromorphic computing have been gaining importance. Within the neuromorphic computing domain, switching of the resistance states in the materials as a function of applied voltage occurs due to complex thermal, chemical, and electrical phenomena. Generally referred to as memristors, these devices can be categorized as the Mott type (e.g., NbO_x),[1] intercalation type (e.g., $LiNbO_x$),[2] or resistive switching type (e.g., HfO_x and TaO_x).[3,4] While the transport phenomena within these materials in the presence of an electric field and an induced thermal field are remarkably different, the core principle behind the operation of memristors is the ability to tune the electrical resistance of the material using an applied electric field alone. Since mass transport is involved in the fundamentals of the switching mechanism, there is a coupled dependence of the behavior between the applied electric field, the diffusion of ions, and the thermal fields. This alone can be greatly impacted by the device geometry along with thermophysical and mass transport properties of the materials in the memristor devices. In order to understand the switching behavior of memristor devices, it becomes essential to study the underlying transport phenomena so that the internal resistances of these materials can be accurately controlled through the creation of appropriate device architectures

along with the application of the appropriate electrical and thermal environments.

Among neuromorphic computing solutions, switching mechanisms observed in Resistive Random Access Memory (ReRAM) devices (HfO_x) are particularly interesting. When a positive bias is applied across the HfO_x layer, a metal-like filament forms to achieve the on-state (set stage), yet the filament is suppressed gradually as the polarity is reversed (reset). A gradual resistance change during both reset and set is desirable, yet the analog characteristic during the reset is very crucial for HfO_x memristors, because multiple resistance states can be accessed via specific terminal voltages during the reset. This type of switching is attributed to oxygen vacancies[3–7] and their movement within the filament, as shown in Fig. 1(a), which is intimately dependent on favorable temperature and electric fields. Therefore, controlling the distribution and removal of heat from these devices is essential to attain a desired non-volatile memory state of the material.

The devices analyzed in this work were fabricated on silicon or glass substrates (vastly different thermal conductivities: 146 W m^{-1} K^{-1} and 1.1 W m^{-1} K^{-1}, respectively) with successive depositions of gold (Au) bottom electrodes (BEs), HfO_x layer, Ti oxygen reservoir layer, and followed by the Au top electrode (TE), as shown in Figs. 1(b) and 1(c) (see the section titled "Methods"). In a fresh device, under a positive bias, Hf and O in HfO_x separate to form oxygen vacancies. Oxygen ions move toward the TE or the positive electrode and temporarily react with the Ti layer. When multiple vacancies form a conducting filament (CF) of oxygen vacancies, breakdown is said to have occurred resulting in an on-state of the device at the formation voltage, which is typically around 4 V and above. In some cases, excess oxygen bubbles out at the interface between Ti and Au, therefore, degrading the device. However, this phenomenon was not observed at smaller voltages pointing to the robustness of the HfO_x devices.

When the polarity on the TE reverses to a negative voltage, a few oxygen ions move back into the filament to neutralize the vacancies, thereby, creating a dielectric barrier of a few monolayers. This causes the breakup of the CF, and the electrical conductivity of the HfO_x layer decreases, resulting in an off state. Finally, when the voltage at the TE is reversed to positive, a much smaller voltage (e.g., 0.5 V) is enough to reduce a few monolayers of HfO_2 to regain the conducting path, and the on-state is re-established or the filament is "set."

Depending on the magnitude of the negative voltage applied during the reset stage, multiple resistance states can be accessed; therefore, understanding the factors affecting the set/reset switching performance and how best they can be controlled with the least amount of energy is of immense interest to the memristor community.

Several models have been put forth in the past to describe the *I–V* characteristics of memristors, which give varying emphases to the electric and thermal field predictions. In general, these categories are: spatially averaged heat transfer and current flow,[8–10] decoupled thermal and current analyses,[11] barrier modulation as a function of oxidation length,[12–17] one-dimensional movement of oxygen vacancies and heat transfer,[18–20] 2-D axisymmetric vacancy, current and energy transport,[3,4,6,7,21] multi-phonon Trap Assisted Tunneling (TAT),[5,22–24] and Density Function Theory (DFT).[25] Among them, the spatially averaged variable approach and decoupled electrical and thermal field simulations are inaccurate in terms of physical principles, and the barrier modulation approach does not fully resolve the integral transport processes. The barrier modulation is a generalized approach that involves the variation of a weighted function or a Schottky barrier as a function of applied voltage, wherein movement of oxygen vacancies is not tracked. The 2-D axisymmetric variation of oxygen vacancies, current, and thermal energy transport is superior to its 1-D counterpart, yet the models described in the literature do not assume realistic thermal boundary conditions and completely ignore the effect of the thermal boundary interface or substrate materials. For instance, assuming the electrodes to be at a constant temperature of 300 K is highly inaccurate and very difficult to create in an actual experiment.[3] The DFT and TAT techniques are advanced in terms of evaluating electron–phonon interaction and subsequent determination of activation

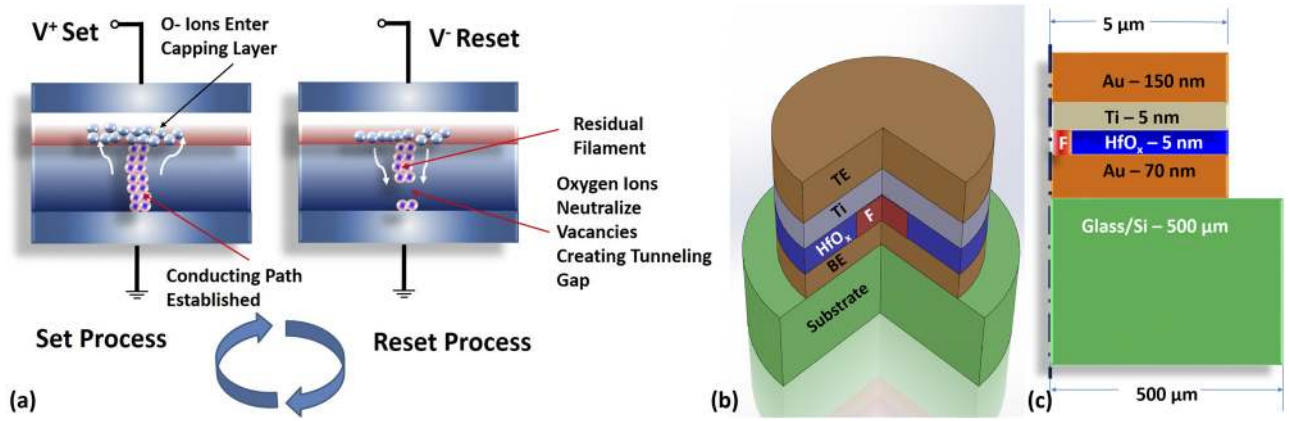

FIG. 1. (a) Set and reset stages involved in DC bias experiments for filamentary memristors, showing mechanisms responsible for switching. (b) Axisymmetric cross section of the device considered for the simulations and experiments. F represents the filament cross section. (c) Dimensions of the material layers used in the experiments and the models.

energies, yet scaling them to device relevant length scales is computationally expensive and impractical, considering that the length scales, which we wanted to explore in the same simulation, range from 1 Å to 1 mm.

The goal of this study was to understand the field-related mechanisms that control the resistance states and current flow in HfO_x and develop a model that can be used to predict the device behavior based on the device architecture. Therefore, the present modeling approach accounted for the drift, diffusion, and thermophoresis of oxygen vacancies in radial and axial directions and accounts for the current flow and heat transfer at all locations. This enabled parametric studies to assess the effect of substrate materials, input voltages, and voltage ramp rates on measurable device temperatures and current magnitudes. In this study, computational modeling efforts were undertaken to simulate the set and reset behaviors in HfO_x filamentary memristors, the schematics of which are shown in Fig. 1(a).

While the filament temperature is difficult to measure for a vertically stacked device, this model opens avenues to predict the device surface temperature and compare it with the measurable parameters. With validation, the model will uniquely provide the potential to design the architecture of filamentary devices for a specific switching behavior.

MODEL DEVELOPMENT

The governing equations solved to generate nanoscale to macroscale electric and thermal fields were oxygen vacancy conservation (n_V), current (I), and thermal energy conservation. They were intimately coupled through electrical conductivity (σ) and thermal conductivity (k) as a function of oxygen vacancy density (n_V) and temperature (T). They are shown in Eqs. (1)–(3), respectively,

$$\frac{\partial n_V}{\partial t} + \nabla \cdot (v_V n_V) = \nabla \cdot (D_V \nabla n_V) + \nabla \cdot (S_V D_V n_V \nabla T), \quad (1)$$

$$\nabla \cdot (\sigma \nabla \psi) = 0, \quad (2)$$

$$\frac{\partial T}{\partial t} = \frac{1}{\rho c} \nabla \cdot (k \nabla T) + \frac{\sigma}{\rho c} (\nabla \psi)^2. \quad (3)$$

In these equations, ψ is the potential, ρ is the density, and c is the specific heat of materials.

It may be noted that the number of oxygen vacancies were chosen for the conservation instead of oxygen ions because electrical conductivity of the material is proportional to the number of vacancies. Therefore, it was straightforward to use a simple correlation between them that will be described later.

These three conservation equations were solved for three different overlapping domains, as shown in Fig. 2. The vacancy conservation equation was solved for the pure Ti and HfO_x domains including the filament. The Au electrode layers do not interact with vacancies or oxygen ions; hence, they are bound by the boundaries with the gold electrodes. Accordingly, the boundary condition for the vacancy conservation is shown in Fig. 2 (top).

The electric current conservation equation was solved for the two electrodes along with the conducting filament, insulating HfO_x and the pure Ti layer, as shown in Fig. 2 (middle). The boundary conditions for this equation were the voltage bias applied at the top of the TE and ground at the bottom surface of the BE. The rest of the boundaries of the domain were electrically insulating.

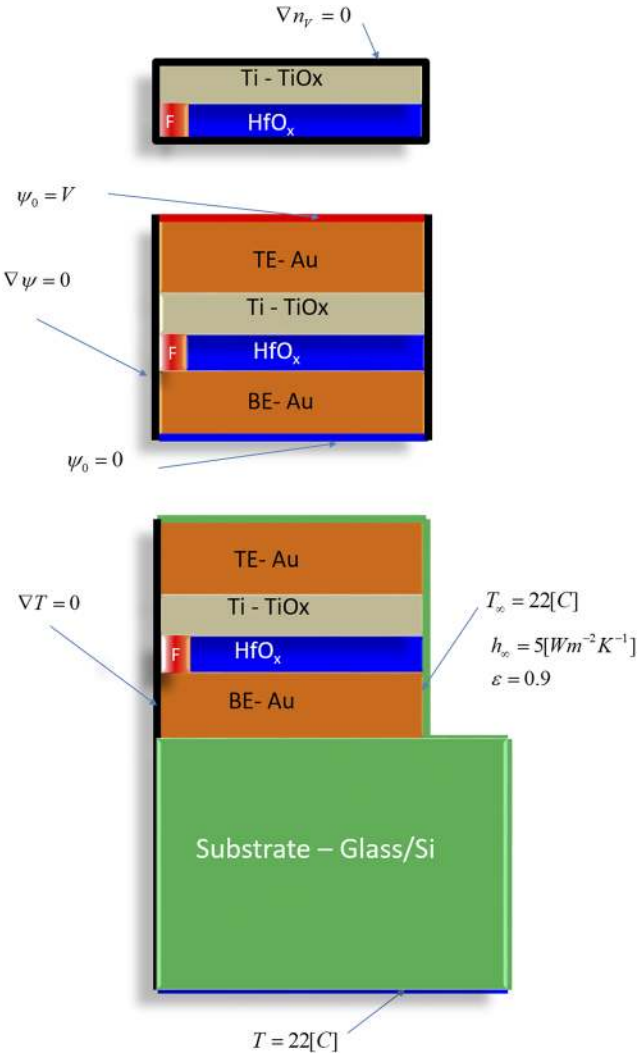

FIG. 2. Boundary conditions for oxygen vacancy conservation (top), current conservation (middle), and energy conservation (bottom).

Finally, the energy conservation was solved throughout the geometry, including the substrate. The surfaces of the stack that are exposed to the ambient were assumed to reject heat via convection and radiation with the assumed ambient temperature of 22 °C. The bottom of the substrate is also fixed at 22 °C, through which the heat is removed from the system, as shown in Fig. 2 (bottom). It was assumed that the substrate was in perfect contact with an infinite heat sink kept at 22 °C.

The critical parameters for this simulation, which govern the solution of the conservation equations, are the electrical conductivity (σ), thermal conductivity (k), oxygen vacancy drift velocity (v_V),

diffusion coefficient of oxygen vacancies (D_V), and thermophoresis coefficient (S_V), and Eqs. (4)–(7) show the equations used to estimate these properties,

$$\sigma = \frac{(\sigma_{HfOx} - \sigma_{HfO_2})}{n_{V,Max}} n_V e^{\left(-\frac{E_{AC}}{k_B T}\right)}, \tag{4}$$

$$k = k_{HfO_2} + \frac{(k_{Hf} - k_{HfO_2})}{n_{V,Max}} n_V, \tag{5}$$

$$v_V = fa \times e^{\left(-\frac{E_a}{k_B T}\right)} \times \sinh\left(\frac{-qa\nabla\psi}{k_B T}\right), \tag{6}$$

$$D_V = \frac{fa^2}{2} \times e^{\left(-\frac{E_a}{k_B T}\right)}, \tag{7}$$

$$S_V = -\frac{E_a}{k_B T^2}. \tag{8}$$

The constants used in these equations are listed in Table I.[3–5,26]

While the thermophysical properties such as σ and k are usually constant for a material, their sudden variation as oxygen vacancies move is the core principle behind this simulation. It must be noted that in sub-stoichiometric HfO_x, (1 − x) represents the amount of vacancies. Hence, the initial value of the vacancy density is based on the experimentally determined value for x of 1.82. Depending on the movement of vacancies tracked in the simulations, x changes locally; however, its value is not tracked explicitly. For instance, when the conducting filament is formed, the electrical conductivity is high. Electrical conductivity is conversely lowered, when oxygen ions neutralize the vacancies and insulating regions are formed. It was assumed that the electrical conductivity was linearly dependent on the vacancy density as shown in Eq. (4), while the temperature dependence was considered using an activation energy for conduction (E_{AC}).[3,4] This behavior is consistent with that of an insulator, wherein the temperature dependence is enhanced through mechanisms such as Poole–Frenkel, when the number of vacancies is small. However, the temperature dependence is diminished, when the material regains a metal-like filament.[3,4] Figure 3(a) shows the variation of E_{AC} with the vacancy density, which agrees with the description. As a result of the E_{AC} variation, σ curves show the variation shown in Fig. 3(b). The temperature dependence at the low vacancy density is significant due to high E_{AC} and vice versa.

TABLE I. Constants and physical properties used in set/reset simulations.

Parameter	Value
$n_{V,Max}$	2×10^{27} m^{-3}
F	2×10^{10} Hz
a	10^{-10} m
E_a	1.5 eV
$E_{AC,Max}$	0.125 eV
ρ	9680 kg m^{-3}
C	60 J kg^{-1} K^{-1}
k_{HfOx}	5 W m^{-1} K^{-1}
k_{HfO2}	0.5 W m^{-1} K^{-1}

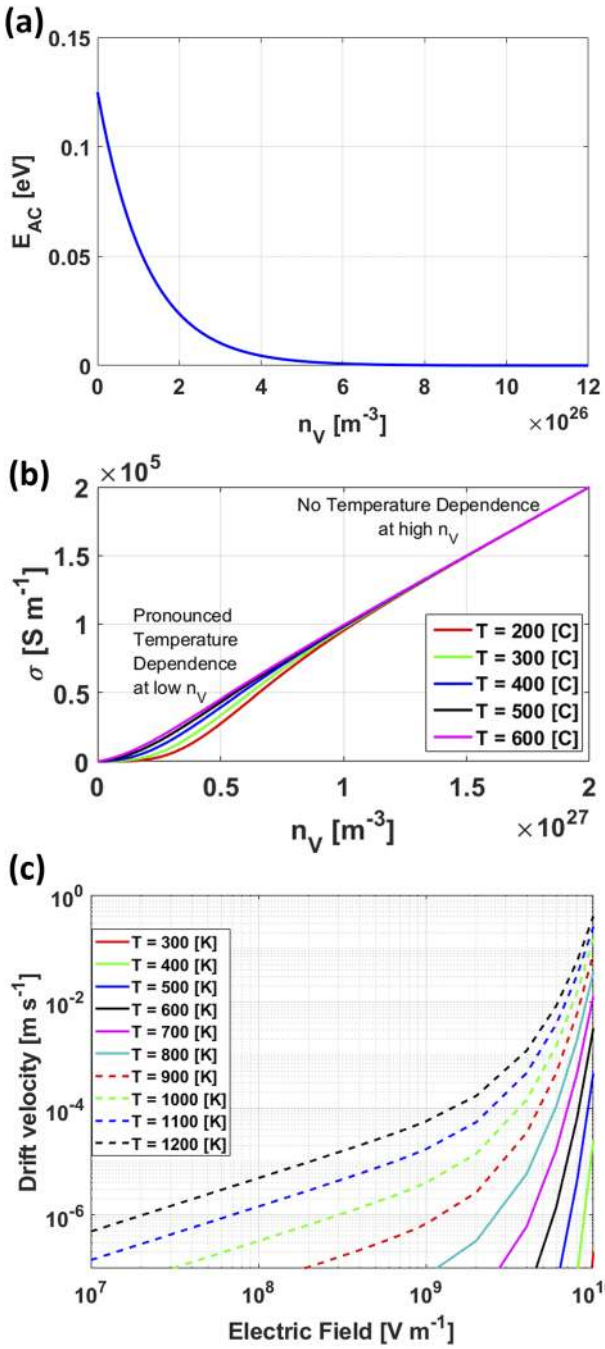

FIG. 3. (a) Variation of activation energy for conduction with vacancy density. (b) Variation of electrical conductivity with vacancy density showing temperature dependence. (c) Drift velocity as a function of electric field and temperature.

Another important aspect of this simulation was the selection of numerical values of σ and k for the capping layer and HfO_x for a thickness of 5 nm. At these small length scales, phonon contributions toward heat transfer are smaller than their electron counterpart. Hence, thermal conductivity values are typically much smaller than that of the bulk material, as seen in Table I.[26]

In addition, when oxygen ions are separated from Hf^{+}, they carry a negative charge. However, it can be safely assumed that they are not the primary charge carriers, as they are trapped in the HfO_x and Hf layers. As defects or vacancies arrange themselves to form a conducting filament, electrons entering the oxide material from the bottom electrode combine with the vacancy and then continue to hop forward, a mechanism that is described in detail by trap assisted tunneling (TAT) models.[5] This means that the behavior of the reduced oxide material is not like a perfect metal, which possesses a cloud of electrons, but is analogous to an intermediate state, where the conductivity is not as high as pure metals. Yet, this intermediate state is not electrically insulating and facilitates the flow of electrons between the two electrodes. Furthermore, the activation energies reported for oxygen ions through the filament once they are created are 0.3 eV, which is less than the reported values for oxygen vacancies (0.7 eV–1.5 eV).[3–5] This means that the movement and rearrangement of oxygen vacancies to facilitate the flow of electrons is the governing phenomenon to conduct electricity, while the movement of oxygen ions is not. Unfortunately, the research on experimental determination of the filament thermal and electrical conductivities is in nascent stages, and researchers have been using techniques such as DFT to investigate internal states of the material, when a vacancy is formed, and how it can help the movement of electrons. Therefore, the value of electrical conductivity of the filament 2×10^5 S/m[3,4] for an n_V of 2×10^{27} m^{-3} [Fig. 3(b)] was chosen based on those used in the literature and validation exercises in this work. It must also be noted that the electrical conductivity value has another controlling element in the models, i.e., the filament diameter, which is described later.

The oxygen vacancy velocity variation with temperature and electric field is shown in Fig. 3(c).[3] It can be noted that the hyperbolic sine function accounts for the variation of the velocity effectively exhibiting a moderate increase in the velocity at small electric fields and a breakdown of the material at high electric fields, showing a sudden exponential increase. This equation is derived based on the approach put forth by Cabrera and Mott[27] to dictate the drift velocity of ions during oxidation.

Finally, this simulation accounts for thermophoresis through S_V, which means that the vacancies migrate from a cold location to a hot location. A reverse direction was considered in at least one study,[6] but is inconsistent with the physics of the problem. This is because mobile ions have more kinetic energy, when they are in the high temperature zone, and tend to move elsewhere to dissipate this heat. As a result, vacancies moving in an opposite direction are aggregated inside the high temperature zone.

The simulation started with the reset/suppression of an already present conducting filament by applying a negative voltage at the TE in the form of a DC sweep up to −1 V, as shown in Fig. 4, for 5 s. It was then followed by a set stage for 5 s, where the suppressed filament regained its conducting behavior after the application of a positive voltage at the TE.

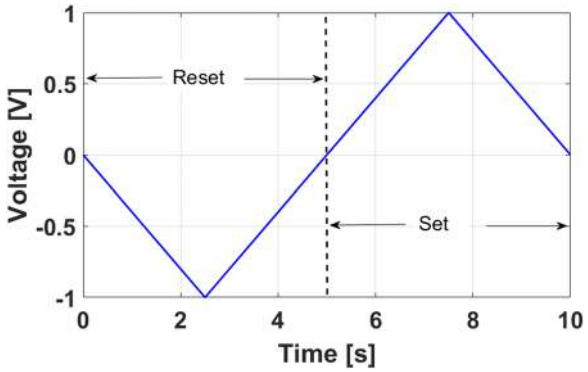

FIG. 4. Voltage input at the TE top surface used as a boundary condition.

FILAMENT INITIAL STATE AND ASSUMPTIONS

In the previous studies, a concrete justification of the initial size of the filament has not been reported. However, with the availability of the experimental *I–V* curve, it was possible to deduce a combination of the slope of electrical conductivity as a function of n_V [Fig. 3(b)] and the filament size, which together yielded the correct *I–V* profile in the on-state of the device. As shown in Eq. (9), for a given electric field (the term in bracket), the total current, *I*, is a function of the product of the electrical conductivity, σ, and the cross sectional area of the filament A. Therefore, without explicit knowledge of the size of the filament, both σ and A together were varied in such a way that the total current, *I*, for a given voltage, *V*, matches with that seen in the experiments for the exact same material structure,

$$I = (-\nabla\psi)\sigma A. \tag{9}$$

Figure 5(a) shows the reset *I–V* curve obtained from the experiments performed on the device with the voltage profile shown in Fig. 4 and a glass substrate. For 100 cycles, current values at the same voltage were averaged to get the mean profile. As shown in Fig. 5(a), the specific features of this curve that the model was expected to replicate during the reset are: the slope of the *I–V* curve (feature 1), the reset onset voltage (feature 2), current at the end of the reset (feature 3), and the off-state curvature (feature 4). Now, as the simulation began in an on-state with the negative voltage applied to the TE, it was imperative that the conducting filament conductivity and size should result in the exact slope of the *I–V* curve. If the filament were any bigger or smaller than the appropriate size, then the slope would change, which would change not only the reset onset voltage marginally, as seen in Fig. 5(b), but also the magnitude of the maximum current dramatically. Therefore, the selection of the filament size and the electrical conductivity is critical for the entire range of the *I–V* curve for a given experiment. In this model, it was assumed that the filament is 4 nm in radius for the listed electrical conductivity in Table I, and it resulted in a good agreement between the test and model results. There could be multiple filaments of smaller size (≈1 nm radii), leading to the cumulative current seen in Fig. 5(c), yet without the experimental evidence of those for the relevant conditions, it was difficult to assume so. In this study, we found only

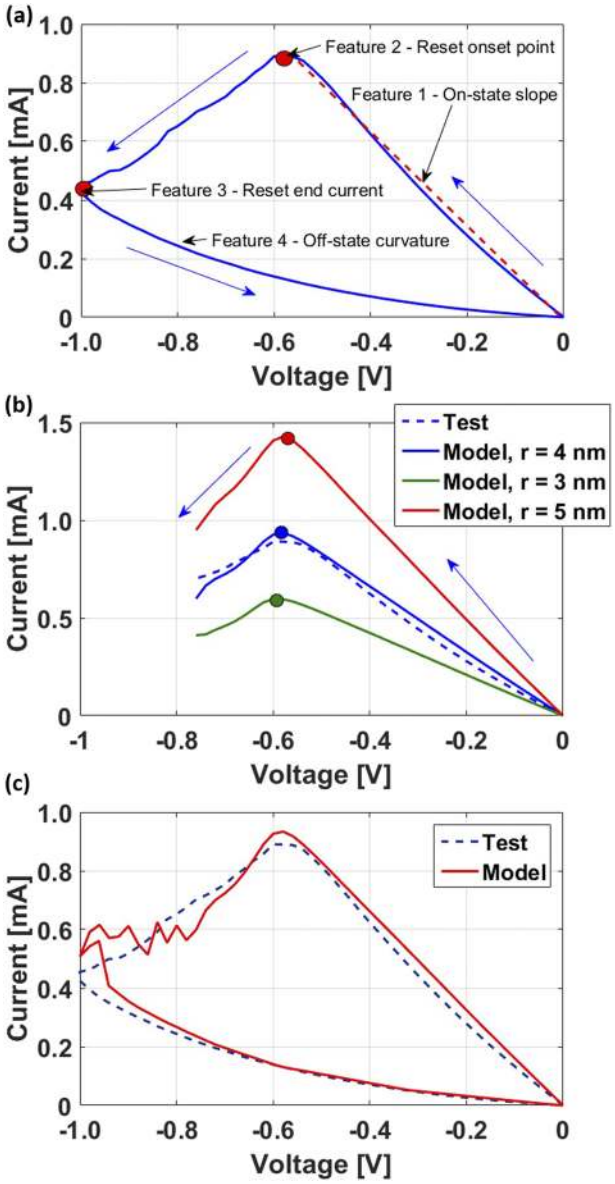

FIG. 5. (a) Features of the *I–V* curves during the reset stage that the model is expected to simulate. (b) Effect of the filament size on the reset *I–V* curves. (c) Model validation for the glass substrate shown during the reset stage.

one filament corresponding to a single hot spot. Therefore, only one filament was considered in this modeling work to have given rise to the on-state of the device.

Finally, the vacancy distribution along the radial direction remains a less studied question and would arise primarily when simulating the current through the filament. Starting at the filament axis, it is not evident whether the vacancy density decays exponentially or along a hyperbolic tangent, etc. Three representative profiles that were used in the simulations are shown in Fig. 6. While there are reports that the radial variation of

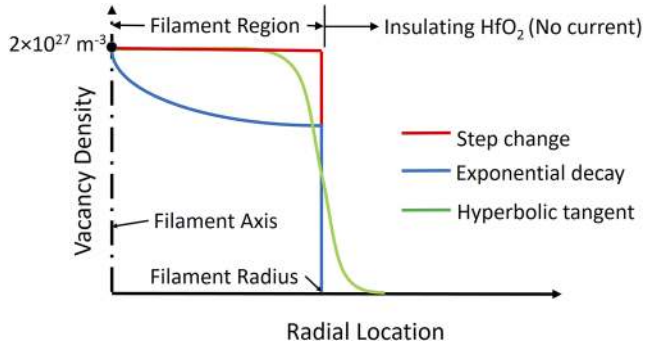

FIG. 6. Radial vacancy variation showing a step change, an exponential decay, and a hyperbolic tangent. Exponential decay is chosen for the simulations.

vacancies does affect the overall results,[28,29] different initial conditions resulted in slightly different reset characteristics and *I–V* plots, and these variations are not discussed here for brevity. However, for this work, the vacancy density was assumed to follow an exponentially decaying profile, which resulted in a better model validation.

The variation of activation energy (E_a) is also important in governing the onset of the reset (feature 2). It is implicit that for a given set of voltage and current values in a given geometry for fixed boundary conditions, the temperature field within the filament is fixed. However, variation of E_a governs as to when the vacancies begin to move. Higher activation energies resulted in a delayed onset of the reset and vice versa. A range of activation energies has been reported in the literature; however, an E_a of 1.5 eV in the present work resulted in the same reset onset voltage of 0.57 V for this device on the glass substrate.

Once these three major checks (filament size, radial vacancy variation, and Ea) were cleared, the rest of the features of the I–V curve were taken care of by the model without any manual interventions. As shown in Fig. 5(c), the I–V curves from the model and the tests were in near perfect agreement and were well within the error margins of the experiments, which validates all the assumptions used in the model. The rest of the two features, namely, the current at the end of the reset and the off-state curvature were appropriately predicted by the model. Then, model variables such as temperature and vacancy contours were used to draw useful insights into the operation of the HfO_x memristors.

RESULTS AND DISCUSSION

This model was used to simulate the reset and subsequent set stage of the device between the voltage windows from −1 V to +1 V, on an already formed filament. Figure 7 shows the contours of n_V and T fields in the filament and surrounding region for a glass substrate at the end of the reset stage. Please note that these are axisymmetric contours of a cross section, the horizontal direction is radial, and the vertical direction is along the filament axis.

As a negative voltage bias across HfO_x increases, the positively charged oxygen vacancies are attracted toward and pile up near the negative electrode (TE), and thereby, their density near the TE

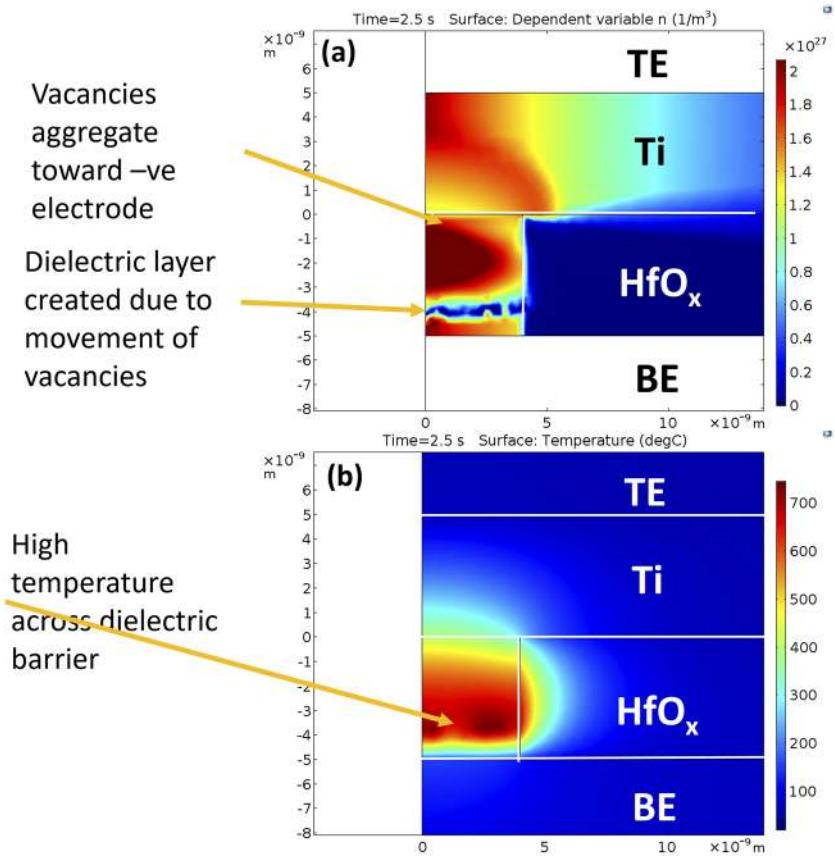

FIG. 7. (a) Vacancy density. (b) Temperature at the end of the reset stage for the glass substrate.

increases. This creates a depleted vacancy region or a dielectric layer near the BE, as shown in Fig. 7(a). As the vacancy density decreases, the electrical conductivity and current density both decrease. Due to the local change in electrical conductivity, the voltage gradient across this barrier is high and creates two distinct layers. Simultaneously, as the vacancy barrier is created, the temperature across it increases compared to the conducting region of the filament, as shown in Fig. 7(b). Thermophoresis then causes the vacancies to be attracted to the high temperature region, resulting in two counteracting phenomena: vacancies move toward the TE due to the drift, while high temperature attracts them back into their original position due to thermophoresis. This results in the fluctuating current profile seen consistently with reset experiments.

After the targeted reset voltage of −1 V is achieved, the decreasing voltage merely lowers the current density and temperature without any significant change in the material properties of HfO_x and a high resistance state (HRS) is created. At the end of the reset, the vacancy distribution stabilizes [Fig. 7(a)] because the increasing negative voltage driving force no longer exists. As the barrier is created becoming a bottleneck for the current flow, it has a smaller n_V as compared to its surroundings. As the voltage approaches zero on the reset side, the temperature of the filament is not high enough to enable the movement of vacancies; thus, the current and temperature fall without further changes to the vacancy density field.

As the TE voltage increases in the positive direction during the set stage, the oxygen ions are attracted toward the TE. While staying in the high resistance state, the current gradually increases until the set voltage is achieved. The set voltage is automatically determined based on the temperature field and is a function of instantaneous thermal and electric fields. Once the electric field reaches a particular range, it is responsible for multiple orders of magnitude increase in the drift velocity [see Fig. 3(c)]; then, due to the combined effect of drift and thermophoresis, the vacancies almost instantaneously (on a voltage scale) rearranged themselves to form a conducting path, as shown in Fig. 8(a). This also means that oxygen ions from the dielectric barrier layer are suddenly moved to the Ti capping layer, which can be seen in the form of a drop in vacancy concentration in the Ti layer.

Unlike during the reset, the drift and thermophoresis act in the same direction during the set. This compounded effect results in a dielectric layer breakdown due to the injection of vacancies. Due to the increase in current, temperature of the conducting path suddenly increases, as shown in Fig. 8(b).

VALIDATION USING ELECTRICAL AND THERMAL EXPERIMENTS

Concomitant changes in the total current measured between the electrodes as a function of voltage are shown in Fig. 9(a). As

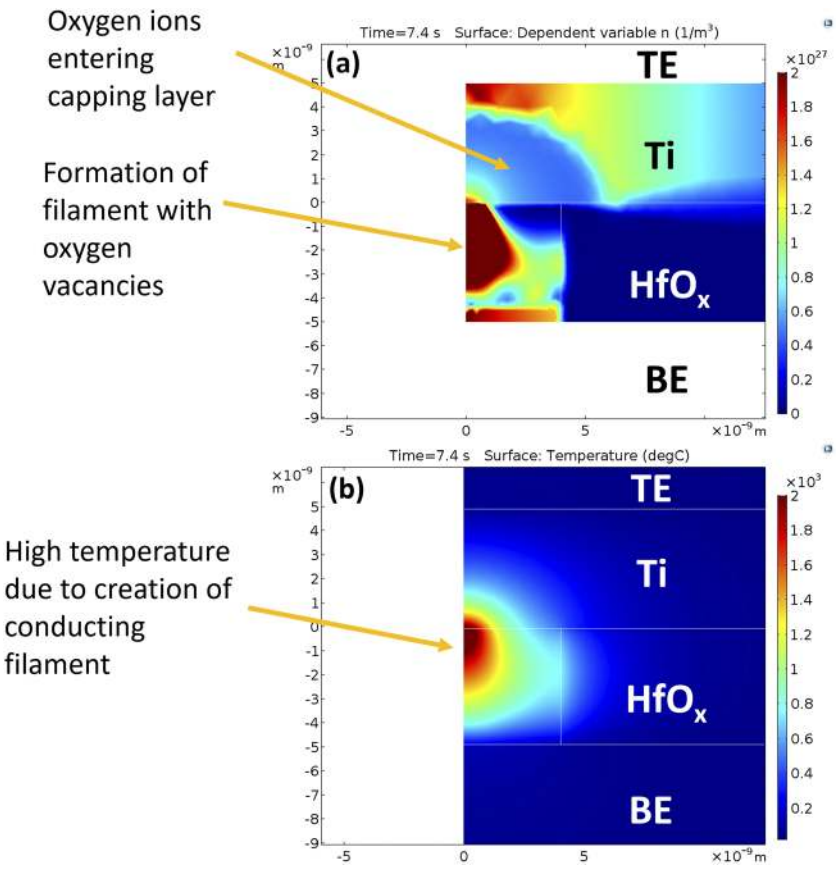

FIG. 8. (a) Vacancy density. (b) Temperature at the end of the set stage for the glass substrate (when the filament has set).

the simulation starts in the on-state with a negative bias at the TE, I–V characteristics are linear as expected until the current begins to drop due to the onset of the reset (upward arrow on the reset side). The movement of vacancies results in a gradual or analog drop until the reset is interrupted at the final reset voltage. In the next phase of the reset process, the current simply drops as the voltage drops due to the formation of a low n_V barrier. As the temperature begins to decrease, the electrical conductivity decreases resulting in a decrease in the current. This in turn results in a decrease in energy dissipated and the device temperature. As a result, the I–V plot shows a curvature in the off state during both the reset and set seen for the HRS on the reset and set sides. At the set voltage, the filament regains its conductive nature and the current increases digitally.

To study the impact of the thermal conductivity of the device substrate on the set–reset behavior, simulations were performed for HfO_x on glass and silicon substrates and the I–V responses were experimentally validated, as also shown in Fig. 9(a). For both substrate materials, the average deviation between the model results and experimental I–V curves was smaller than 8.5%, except for the set voltage data points. During the set, a device shows randomness in the voltage at which it regains the on-state. This randomness is shown in Fig. 9(b), which shows the range of set voltages for a sample device from 0.45 V to 0.90 V.

The resistance ratio for the glass substrate [ratio of electrical resistance in the high resistance state over that of the low resistance state (LRS) for the reset voltage of −1 V measured at 0 V] was 10.5 as predicted by the model, while that observed in the experiments was 12.7, as shown in Table II, and the agreement is similar for the Si substrate. This comparison indicates that the glass substrate yields a marginally greater memory window, as seen in Fig. 9(a) and from the resistance ratios. This is attributed to a greater mobility of oxygen vacancies, which in turn is dependent on heat remaining trapped in the filament for glass substrates due to their lower thermal conductivity and discussed in detail later. Please note that the resistance ratios are measured at 0 V, while the standard deviation of 8.5% is calculated at all data points.

The coupled model was also used to predict the I–V curves, n_V, and T fields as a function of voltage ramp rates. This was important to understand the effect of the drift field time scale on temperature field and vice versa. As the ramp rate increases, the time window available for the movement of the vacancies becomes narrower.[4] Therefore, the voltage required for the onset of the reset increases with the ramp rate. This results in the device staying in the on-state for a broader voltage window during the reset, as seen in Fig. 10(a), subsequently raising the temperature of the filament tip to increasingly higher values. Another consequence of increasing the voltage ramp rate is the narrowing of the memory window for a given end

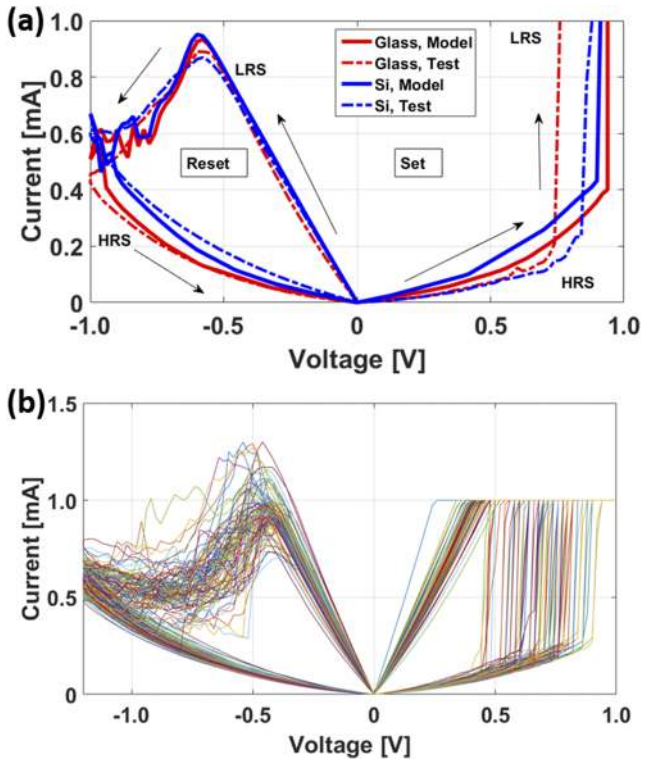

FIG. 9. (a) Model *I–V* curve showing the reset and set stages with a low resistance state (LRS) and a high resistance state (HRS) simulated for glass and Si substrates. The cycle is 10 s long with a voltage ramp rate of 0.4 V s^{-1}. (b) A set of experimental *I–V* curves for a glass device showing randomness associated with the reset and set and variation of the onset of the reset voltage and set voltage.

reset voltage. While the onset of the reset is delayed on a voltage scale for an increased ramp rate, the off-state resistance achieved at the fixed reset voltage is higher than that for a lower ramp rate. For a ramp rate of 0.4 MV s^{-1}, the reset process could not commence, and the device stayed in the on-state for a reset/set window of ±1 V. It is interesting to note that the filament tip temperatures qualitatively followed the *I–V* curves for the corresponding voltage ramp rates. While the results in Figs. 10(a) and 10(b) are shown for a glass substrate, they are similar for the Si substrate. It could be argued that a steeper ramp rate would amplify the effect of trapped heat on vacancy movement. However, the vacancy movement itself at a high voltage ramp rate is arrested as a result of insufficient time. Therefore, any augmentation of trapped heat due to short cycles is neutralized by marginal or insignificant movement of vacancies, resulting in a minor difference in the *I–V* plots for the two substrates. Such a substrate dependent behavior has been experimentally studied and reported by the authors previously.[30,31]

TABLE II. Resistance ratios for glass and Si substrates predicted by models and observed in tests.

	Glass	Si
COMSOL model	10.5	8.9
I–V experiments	12.7	5.7

Figure 10(c) sheds more light on competitive time scales for ion movement and heat transfer through glass and Si substrates. Glass dissipates heat more slowly than Si due to its smaller thermal diffusivity; therefore, it shows the onset of the reset marginally earlier than that in the Si (≈0.05 V). This is because the temperature at which the vacancies become mobile is achieved earlier during ramping the voltage up. This initial difference in the *I–V* for the substrates results in subsequent differences in different off-state resistances for them.

However, this difference is far less significant than anticipated, if only thermal diffusivities of these materials are considered. This is because of the similar volumetric heat capacities of these materials (1.68 MJ m^{-3} K^{-1} and 1.63 MJ m^{-3} K^{-1} for glass and Si, respectively). With a large substrate volume available for the heat to be stored as it is generated, the ability of the thermal conductivity of the material to remove the heat quickly or slowly is suppressed. Therefore, the difference in *I–V* curves for these two substrates for the same voltage ramp rates is not remarkable.

However, the *I–V* curves for glass and Si both shift in a similar way significantly, as seen in Fig. 5(c), when the total cycle time for the reset/set is changed to 0.1 s, making the voltage ramp steeper. While heat transfer through substrates is equally affected by this change, the ion movement does not initiate after a significant rise in temperature due to lack of enough time. Therefore, the time required for the movement of ions/vacancies was determined to be the governing factor in determining the onset of the reset. It must be noted that the drift velocities for vacancies were of the order of 1 nm s^{-1} at 1000 K and an electric field of 10^8 V m^{-1} [when 0.5 V is applied across 5 nm thick HfO_x, Fig. 3(c)]. This is significantly small to achieve any rapid changes in the filament structure during the reset stage (note that the drift and thermophoresis act in opposite directions during the reset, so an even greater drift velocity is required to compensate for thermophoresis). Therefore, for steeper ramps, although the voltage changed with time rapidly with the time scale of the order of milliseconds, vacancies did not begin to move because the drift time scale was much longer.

The use of different substrates, however, alters the fraction of heat going toward the TE vs the BE. As a result, the TE dissipates more heat in the case of the glass substrate, when compared with the Si substrate. This creates different thermal fields elsewhere in the devices away from the filament, yet the filament thermal field remains mostly unaffected as seen from the temperature and vacancy contour plots for these two substrates. Measurement of the TE surface temperature experimentally for the two substrates provides a second tier for the validation of this electrothermal model.

The technique employed for the temperature measurement was the transient thermoreflectance imaging (TTI) system (Microsanj™ NT 210B). Transient thermoreflectance imaging uses the temperature dependent reflectivity of the surface in order to measure the temperature in the devices. A 470 nm LED was used as the illumination source during device operation. This wavelength is chosen to capitalize on the high sensitivity of the thermoreflectance coefficient of Au. A CCD camera was used to measure the

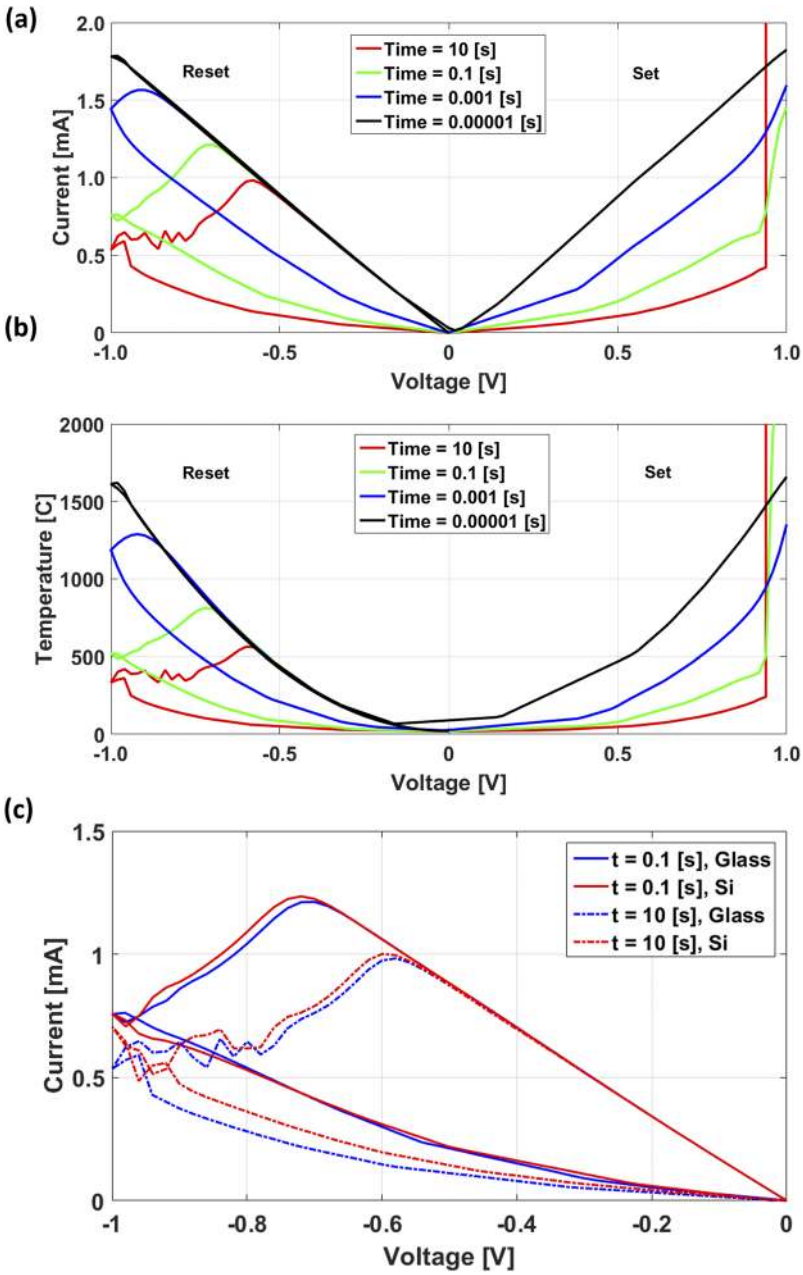

FIG. 10. (a) *I–V* plots and (b) filament tip temperature variation for voltage ramp rates of 0.4, 40, 4000, and 400 000 V s^{-1} for a glass substrate. These ramp rates correspond to the total reset–set cycle times of 10 s, 0.1 s, 0.001 s, and 0.000 01 s. (c) *I–V* plots for glass and Si substrates compared for 10 s and 0.1 s cycle time.

thermoreflectance signal with a 53.5 nm/pixel resolution.[32] Under the test conditions used, the temperature resolution was 0.25 °C with a temporal resolution of 50 ns.

For the temperature measurement, the HfO_x devices were electroformed and the filament was stabilized by alternately resetting and setting the filament for 20 cycles for a reset voltage of −1.5 V and a set voltage of 1.2 V. Then, positive electrical pulses were sent through a set filament, which then raised the temperature of the filament and its surroundings during each pulse. The voltage pulse magnitude was selected such that the total electrical power going through the filament was 1 mW. Negative pulses would increase the resistance of the filament during each pulse; therefore, the visible temperature would drop for successive pulses. However, the Microsanj TTI requires the current to be the same for all pulses to accurately average the temperature of the surface for several pulses. Therefore, negative pulses were not used.

Figures 11(a) and 11(b) show the temperature of the TE surface for the glass and Si substrates measured using TTI at the end of a 100 μs pulse for a 1 mW power flowing through the filament. Three other devices on each substrate showed a very similar temperature

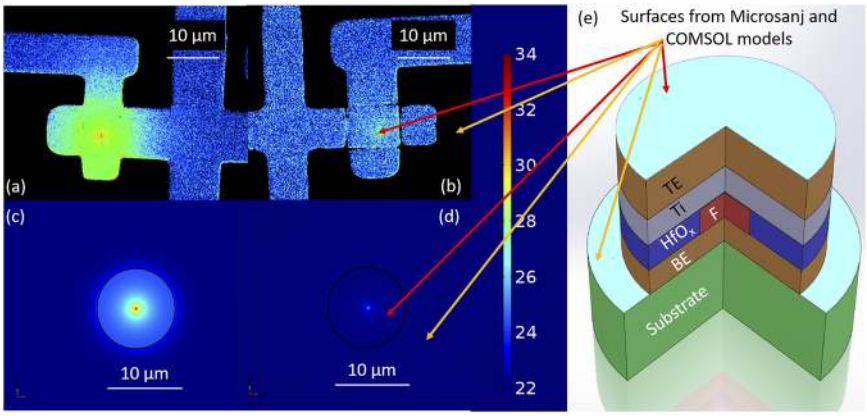

FIG. 11. Temperature contour of the TE surface measured by the TTI method for (a) glass and (b) Si substrates for an electrical power of 1 mW in the on-state (set stage of the filament). Temperature field predicted by the electrothermal model for the same conditions for (c) glass and (d) Si substrates. Temperature units are Celsius. The device boundary is shown by black solid lines for the temperature contours from the model. (e) Blue highlighted surfaces show the visible surface in the measurements and those considered in the model.

rise; however, only one representative image for each substrate is shown. The temperature rise for the TE surface for glass is 11.5 °C, while the same is only 4 °C for Si. It is also apparent that the hot spot is larger for glass than that for Si, clearly validating the fact that a large fraction of heat enters the TE for glass substrates.

The COMSOL electrothermal model was simulated for the same electrical power to flow through the filament, and the temperature of the TE surface was plotted for glass and Si at the end of a 100 μs pulse in Figs. 11(c) and 11(d). Please note that the COMSOL simulation for this validation exercise is different from the previously shown results in Fig. 9 because the ion movement and vacancy density variation in this simulation are not considered. The goal of this simulation was to observe the evolution of the thermal field for a given electrical power so that the observable temperature rise in the top electrode can be predicted and compared with experiments. Please also note that the filament is at the center of the geometry, which is attributed to the 2-D axisymmetric nature of the simulation. The agreement between the maximum temperature of the hotspot and its appearance predicted by the model and those observed experimentally for both substrates is good. The COMSOL model shows the temperature rise for glass and Si as 12 °C and 4.3 °C. Please note that this difference is clearly due to the fractions of the generated heat going toward the TE and BE and not the filament temperature. For the same initial conditions, the temperature fields within the filament in the on-state for both substrates are similar. For the glass substrate, both the model and test results showed that the entire device heated up due to heat spreading in gold, whereas due to the miniscule fraction of heat entering the TE for the Si substrate, the hot spot was smaller in both the temperature magnitude and the spatial distribution. This two-tier model validation is unprecedented for the HfO_x devices to our knowledge, emphasizing the utility of such a model to predict macroscale current and temperature fields.

CONCLUSIONS

In conclusion, we showed that a theoretical model that predicts the drift, diffusion, and thermophoresis of the oxygen vacancies, when solved together with current and energy conservation applied over the complete geometry and realistic boundary conditions, has the potential to predict the behavior of HfO_x filamentary memristors. The I–V curves predicted by this model match with the measured data within 8.5% for glass and Si substrates. Increasing the voltage ramp rate was found to delay the onset of the reset process due to an increasingly smaller time available for vacancies/ions to migrate. In turn, this was found to decrease the memory window of the device. Therefore, the selection of ramp rates is recommended to be based on the available timeframe and required memory states. The substrate material was found to affect the reset and set processes marginally, wherein the low thermal conductivity glass substrate was able to provide a greater memory window and a greater on-state to off-state conductance ratio than those of high thermal conductivity substrate materials.

These results were also validated using transient thermoreflectance imaging of the surface of the top electrodes, and the temperature rises observed for glass and Si substrates matched very well with the predicted surface temperatures. Such a unique multiple-tier validation of the model warrants its use to analyze multiple intermediate variables involved in the operation of filamentary memristors for different input conditions such as second order filament activation, pulsed voltage inputs, and subsequent switching conditions. These results are expected to provide useful insights into the operation of the filamentary memristors and assist with the neuromorphic circuit designs.

METHODS

Device fabrication

The test devices were fabricated on about 2″ × 2″ square size cleaned glass (Gold Seal Catalog No. 3010) and thin surface oxidized-SiO_2 (280 nm)/Si (Orientation: ⟨100⟩) substrates. As mentioned above, isolated crossbar devices of size 10 × 10 μm^2 [*see* Fig. 1(b)] were fabricated using a well-known mask-less lithography approach. Both the BE and TE layers were deposited using a 99.999% Au source at ultra-high vacuum (~3 × 10^{-6} Torr), and the Ti layers were deposited without breaking the vacuum using 99.95% Ti source pellets (Kurt J. Lesker). Note that the 20 nm adhesion layer of the Ti film, i.e., underneath the BE, was deposited to improve the adhesion of the Au layer. The active layer (~5 nm HfO_x) was synthesized using thermal atomic layer deposition (ALD) (45 cycles at 250 °C) with the precursors Tetrakis (dimethylamido)

hafnium (TDMA-Hf) and deionized water. Then, the as-prepared devices were characterized for the electrical properties without any post-fabrication treatments.

ACKNOWLEDGMENTS

Authors would like to thank the Air Force Office of Scientific Research for their funding and support (Grant No. FA9550-18-1-0024).

The data that support the findings of this study are available within the article.

NOMENCLATURE

a	vacancy hopping distance, m
BE	bottom electrode
c	specific heat, J/kg K
D	diffusion coefficient, m^2/s
E	activation energy, J
f	hopping frequency, Hz
F	filament
I	current, A
k	thermal conductivity, W/m K
K_B	Boltzmann constant, J/K
n	concentration, $/m^3$
S	thermophoresis coefficient, /K
t	time, s
T	temperature, K
TE	top electrode
v	oxygen vacancy drift velocity, m/s

Greek symbols

P	mass density, kg/m^3
ε	material permittivity, F/m
σ	electrical conductivity, S/m
ψ	voltage potential, V

Subscripts

a	activation of vacancies
AC	activation for conduction
O	to Hf atomic ratio, generally indicating the presence of a vacancy if less than 2
V	oxygen vacancies

Superscripts

+	positive
−	negative

REFERENCES

[1] S. Kumar, Z. Wang, N. Davila, N. Kumari, K. J. Norris, X. Huang, J. P. Strachan, D. Vine, A. L. D. Kilcoyne, Y. Nishi, and R. S. Williams, Nat. Commun. **8**(1), 658 (2017).

[2] C. Yakopcic, S. Wang, W. Wang, E. Shin, G. Subramanyam, and T. M. Taha, paper presented at the 2017 International Joint Conference on Neural Networks (IJCNN), 2017.

[3] S. Kim, S. Choi, and W. Lu, ACS Nano **8**(3), 2369–2376 (2014).

[4] S. Larentis, F. Nardi, S. Balatti, D. C. Gilmer, and D. Ielmini, IEEE Trans. Electron Devices **59**(9), 2468–2475 (2012).

[5] G. Bersuker, D. C. Gilmer, D. Veksler, P. Kirsch, L. Vandelli, A. Padovani, L. Larcher, K. McKenna, A. Shluger, V. Iglesias, M. Porti, and M. Nafría, J. Appl. Phys. **110**(12), 124518 (2011).

[6] X. Gao, D. Mamaluy, P. R. Mickel, and M. Marinella, ECS Trans. **69**(5), 183–193 (2015).

[7] S. K. Nandi, *Resistive Switching in Transition Metal Oxides for Integrated Non-volatile Memory* (Australian National University, 2017).

[8] P. R. Mickel, A. J. Lohn, C. D. James, and M. J. Marinella, Adv. Mater. **26**(26), 4486–4490 (2014).

[9] M. A. Villena, M. B. González, F. Jiménez-Molinos, F. Campabadal, J. B. Roldán, J. Suñé, E. Romera, and E. Miranda, J. Appl. Phys. **115**(21), 214504 (2014).

[10] M. A. Villena, F. Jiménez-Molinos, J. B. Roldán, J. Suñé, S. Long, X. Lian, F. Gámiz, and M. Liu, J. Appl. Phys. **114**(14), 144505 (2013).

[11] Z. Wang, S. Kumar, H.-S. P. Wong, and Y. Nishi, Appl. Phys. Lett. **112**(7), 073102 (2018).

[12] S. Aldana, P. García-Fernández, A. Rodríguez-Fernández, R. Romero-Zaliz, M. B. González, F. Jiménez-Molinos, F. Campabadal, F. Gómez-Campos, and J. B. Roldán, J. Phys. D: Appl. Phys. **50**(33), 335103 (2017).

[13] T. Chang, S.-H. Jo, K.-H. Kim, P. Sheridan, S. Gaba, and W. Lu, Appl. Phys. A: Mater. Sci. Process. **102**(4), 857–863 (2011).

[14] K. Eshraghian, O. Kavehei, K.-R. Cho, J. M. Chappell, A. Iqbal, S. F. Al-Sarawi, and D. Abbott, Proc. IEEE **100**(6), 1991–2007 (2012).

[15] J. H. Hur, M.-J. Lee, C. B. Lee, Y.-B. Kim, and C.-J. Kim, Phys. Rev. B **82**(15), 155321 (2010).

[16] R. Waser, R. Dittmann, G. Staikov, and K. Szot, Adv. Mater. **21**(25-26), 2632–2663 (2009).

[17] Y. Yang and W. Lu, Nanoscale **5**(21), 10076–10092 (2013).

[18] M. J. Rozenberg, M. J. Sánchez, R. Weht, C. Acha, F. Gomez-Marlasca, and P. Levy, Phys. Rev. B **81**(11), 115101 (2010).

[19] D. B. Strukov, J. L. Borghetti, and R. S. Williams, Small **5**(9), 1058–1063 (2009).

[20] S. Yu and H.-S. P. Wong, IEEE Electron Device Lett. **31**(12), 1455–1457 (2010).

[21] D. Ielmini, Semicond. Sci. Technol. **31**(6), 063002 (2016).

[22] X. Guan, S. Yu, and H.-S. P. Wong, IEEE Trans. Electron Devices **59**(4), 1172–1182 (2012).

[23] F. Jiménez-Molinos, A. Palma, F. Gámiz, J. Banqueri, and J. A. López-Villanueva, J. Appl. Phys. **90**(7), 3396–3404 (2001).

[24] L. Larcher, IEEE Trans. Electron Devices **50**(5), 1246–1253 (2003).

[25] B. Magyari-Köpe, L. Zhao, Y. Nishi, K. Kamiya, M. Y. Yang, and K. Shiraishi, paper presented at the 2014 IEEE International Symposium on Circuits and Systems (ISCAS), 2014.

[26] M. A. Panzer, M. Shandalov, J. A. Rowlette, Y. Oshima, Y. W. Chen, P. C. McIntyre, and K. E. Goodson, IEEE Electron Device Lett. **30**(12), 1269–1271 (2009).

[27] N. Cabrera and N. F. Mott, Rep. Prog. Phys. **12**(1), 163–184 (1949).

[28] S. Tang, F. Tesler, F. G. Marlasca, P. Levy, V. Dobrosavljević, and M. Rozenberg, Phys. Rev. X **6**(1), 011028 (2016).

[29] F. Tesler, S. Tang, V. Dobrosavljević, and M. Rozenberg, "Shock waves in binary oxides memristors," Proc. SPIE **10357**, 103572L (2017).

[30] P. Basnet, D. G. Pahinkar, M. P. West, C. J. Perini, S. Graham, and E. M. Vogel, "Substrate dependent resistive switching in amorphous-HfO_x memristors: An experimental and computational investigation," J. Mater. Chem. C (published online 2020).

[31] M. P. West, P. Basnet, D. G. Pahinkar, R. H. Montgomery, S. Graham, and E. M. Vogel, Appl. Phys. Lett. **116**(6), 063504 (2020).

[32] G. Pavlidis, D. Kendig, E. R. Heller, and S. Graham, IEEE Trans. Electron Devices **65**(5), 1753–1758 (2018).